

Mechanically driven SMR-based NEMS magnetolectric antennas

Xianfeng Liang

Northeastern University

Huaihao Chen

Northeastern University

Neville Sun

Northeastern University

Elizaveta Golubeva

University of Kiel

Cai Müller

Institute for Materials Science, Kiel University

Sushant Mahat

University of Illinois at Urbana-Champaign

Yuyi Wei

Northeastern University

Cunzheng Dong

Northeastern University <https://orcid.org/0000-0002-3379-7816>

Mohsen Zaeimbashi

Northeastern University

Yifan He

Northeastern University

Yuan Gao

Northeastern University <https://orcid.org/0000-0002-2444-1180>

Hwaider Lin

Winchester Technologies

David Cahill

University of Illinois <https://orcid.org/0000-0001-5969-3460>

Mohan Sanghadasa

U.S. Army Aviation and Missile Research, Development, and Engineering Center

Jeffrey McCord

Kiel University

Nian Sun (✉ n.sun@northeastern.edu)

Northeastern University

Article

Keywords:

Posted Date: December 6th, 2021

DOI: <https://doi.org/10.21203/rs.3.rs-1118802/v1>

License:  This work is licensed under a Creative Commons Attribution 4.0 International License.

[Read Full License](#)

1 Mechanically driven SMR-based NEMS magnetoelectric antennas

2 Xianfeng Liang ^{1,*}, Huaihao Chen ^{1,*}, Neville Sun ^{1,*}, Elizaveta Golubeva ³, Cai Müller ³, Sushant Mahat ⁵, Yuyi Wei ¹,
3 Cunzheng Dong ¹, Mohsen Zaeimbashi ¹, Yifan He ¹, Yuan Gao ², Hwaider Lin ², David G. Cahill ⁵, Mohan
4 Sanghadasa ⁶, Jeffrey McCord ^{3,4} and Nian X. Sun ^{1,2,**}

5 ¹ Department of Electrical and Computer Engineering, Northeastern University, Boston, MA 02115, USA

6 ² Winchester Technologies, LLC, Burlington, MA 01803, USA

7 ³ Institute for Materials Science, Kiel University, Kiel, 24143, Germany

8 ⁴ KiNSIS - Kiel Nano, Surface and Interface Science, Kiel University, Kiel, 24143, Germany

9 ⁵ Department of Materials Science and Engineering, Engineering and Materials Research Laboratory, University of Illinois at
10 Urbana-Champaign, Urbana, IL 61801, USA

11 ⁶ U.S. Army Combat Capabilities Development Command Aviation & Missile Center, Redstone Arsenal, AL 35898

12 * Xianfeng Liang, Huaihao Chen and Neville Sun contributed equally to this work.

13 ** Correspondence: n.sun@northeastern.edu; Tel.: +1 (617) 373 3351.

14 **Abstract**—Mechanically driven magnetoelectric (ME) antennas have been demonstrated to be one of the most effective methods to
15 miniaturise antennas compared to state-of-the-art compact antennas. However, the nanoelectromechanical systems (NEMS) ME antennas
16 are fragile due to their suspended thin-film heterostructure, and have very low power handling capabilities. Here we show that solidly
17 mounted resonator (SMR)-based NEMS ME antennas on a Bragg acoustic resonator, which have a circular resonating disk of 200 μm
18 diameters and operate at 1.75 GHz, show a high antenna gain of -18.8 dBi and 1dB compression point (P1dB) of 30.4 dBm. Compared to
19 same-size thin-film bulk acoustic resonator (FBAR) ME antennas with a free-standing membrane, the SMR-based antennas are much
20 more structurally stable with 23.3 dB higher power handling capability and easier fabrication steps. These SMR-based ME antennas are
21 fabricated with processes compatible with complementary metal-oxide-semiconductor (CMOS), exhibiting dramatic size miniaturisation,
22 high power handling, high mechanical robustness, simple fabrication processes, and much higher antenna radiation gain compared to
23 same-size state-of-the-art antennas.

1 **Introduction**

2 In the last few decades, explosive growth in miniaturised, low-profile and cost-effective antennas has emerged due to the proliferation
3 of innovative applications such as Internet-of-Things (IoT) devices, 5th generation (5G) wireless systems, millimetre-wave (mm-
4 wave) and Terahertz (THz) applications, etc.^{1, 2, 3, 4} There is an insatiable need for small-size and highly efficient antennas. Numerous
5 miniaturisation techniques have been developed to reduce the size of antennas, such as loading materials⁵, lumped elements⁶,
6 geometry designs^{7, 8}, metamaterials⁹, etc. However, the dimensions of conventional compact antennas are typically larger than 1/10
7 electromagnetic (EM) wavelength λ_0 ^{10, 11}, which are too large for many current and future technologies, such as implantable and
8 injectable medical devices^{12, 13, 14}.

9

10 Since the renaissance of magnetoelectric (ME) composites in the last twenty years^{15, 16, 17, 18}, different multiferroic devices^{19, 20, 21, 22, 23}
11 have been developed based on the direct (magnetic field control of electric polarisation) or converse (electric field control of
12 magnetisation) ME coupling. The concept of novel ME antennas for antenna size miniaturising has been theoretically proposed²⁴
13 and experimentally demonstrated in the recent past^{25, 26, 27, 28, 29}. In addition to the investigations on ME antennas that operate at very-
14 high frequency (VHF) and ultra-high frequency (UHF) bands, several papers were published on designing mechanical antennas for
15 low frequency (LF) and very-low frequency (VLF) applications based upon a rotating electret or spinning magnet^{30, 31, 32, 33}. In 2020,
16 Dong et al.³⁴ demonstrated a portable and power-efficient VLF communication system with a pair of mechanical ME antennas. The
17 near-field radiation pattern and radiation field distribution in relation to distance were predicted by calculations and confirmed by
18 experiments. The mechanically driven ME antennas are demonstrated to have a much smaller size since they operate at the mechanical
19 resonance, which has about five orders of magnitude shorter wavelength than that of EM resonance at the same frequency.

20

21 Free-standing or released thin-film bulk acoustic resonator (FBAR)³⁵ and solidly mounted resonator (SMR)³⁶ are two principal
22 geometric structures for bulk acoustic wave (BAW) devices to confine acoustic energy in the piezoelectric material. An isolating
23 structure with minimised energy dissipation in the neighbouring media is required to build up a high-quality-factor strong standing
24 mechanical resonance. The acoustic isolation of FBAR is realised by the air gap between the resonating plate and the substrate. At
25 the same time, the SMR uses a Bragg acoustic reflector for confining the mechanical energy in the resonating plate. The Bragg
26 acoustic reflector is composed of alternating layers of low and high acoustic impedance materials with controlled thicknesses. The
27 leakage of mechanical energy is prohibited by the reflection of acoustic waves at each interface of the multilayer stack due to the
28 acoustic impedance mismatch. The disadvantages of these released FBARs include (1) limited thermal dissipation capability and,

1 therefore, low power handling capability, (2) fragile anchors that lead to fracture and low yield rate, (3) tight control of film stresses
2 developing during fabrication and (4) complex fabrication process steps including the releasing processes. On the other hand, the
3 SMR sits on the Bragg acoustic lattice without any suspended structures and has much higher power handling capabilities with simpler
4 fabrication processes and a higher yield rate. The SMR also has much improved mechanical robustness, which allows it to be easily
5 packaged and integrated with integrated circuits (ICs).

6

7 In this paper, we demonstrate a new SMR-based ME antenna to minimise energy loss by returning the vertically propagating energy
8 from the Bragg reflector back to the acoustic resonator. These ME antennas with a $200\text{-}\mu\text{m}$ -diameter circular disk are designed to
9 have a mechanical vibration mode at UHF (1.75 GHz) operation frequencies. Owing to the Bragg acoustic reflector, the SMR-based
10 ME antennas have an antenna gain of -18.8 dBi, comparable to that of the same-size FBAR ME antennas. The 1dB compression point
11 (P1dB) of SMR-based ME antenna was measured to be 30.4 dBm, which is 23.3 dBm higher than that of the FBAR ME antennas
12 with the same size. The combined high power handling capability, high antenna gain, easy fabrication process makes these SMR ME
13 antennas great candidate antennas for different wireless systems.

14

15 **Magnetoelectric composites of the SMR-based ME antenna**

16 The quality of the Bragg reflector sandwiched between the resonator and substrate plays an important role in producing high-class
17 mechanical antennas. The acoustic properties of a variety of materials normally used for modelling and developing Bragg reflectors
18 in SMR devices are measured and summarised (see Supplementary Table 1 and Supplementary Fig. 2). In Fig. 1a and b, the cross-
19 sectional scanning electron microscopy (SEM) image and optical image of the developed ME antenna are presented. The excellent
20 film quality of the Bragg reflector and the ME composite can be seen from these pictures. The signal (S) pad and ground ring (G)
21 structure are used to feed the RF signal into the ME antenna.

22

23 The microstructure, crystal orientation, and piezoelectric properties of ZnO thin films are greatly influenced by the sputtering
24 conditions. We investigated the effects of RF plasma power, sputtering gas pressure, oxygen (O_2) flux density and temperature on the
25 crystal orientation of ZnO films to obtain optimal film properties. During the development of ZnO films, all samples were deposited
26 on the Si substrate and evaluated by x-ray diffraction (XRD) and the full width at half maximum (FWHM) of the rocking curve
27 analysed at the (002) peak. The (002) peak of ZnO and smallest FWHM is around 34.4° and 2.29° , respectively, which indicates good

1 film quality with high c-axis orientation (see Fig. 1c-h). All other samples are amorphous without any ZnO XRD peak that were
2 discovered. The intrinsic stress is one of the most important characteristics for thin-film free-standing membrane ME devices.
3 However, stress optimisation was not as important as the longer necessary due to the inherent durability of SMR devices.

4

5 The magnetic properties of FeGaB/SiO₂ multilayers have been characterised using vibration sample magnetometry (VSM),
6 ferromagnetic resonance (FMR) spectroscopy, and magneto optic Kerr effect (MOKE) imaging³⁷. The results for both a reference
7 sample with 5 mm × 5 mm full film deposited directly on Si substrate and a patterned device with the magnetic stack deposited on
8 the ZnO film are displayed in Fig. 2. All magnetic films were sputtered onto the substrates under an in-situ magnetic field of $H_{\text{in-situ}}$
9 of $\sim 2.4 \times 10^4$ A/m to induce a well-defined in-plane uniaxial magnetic anisotropy (UMA). Fig. 2a and d illustrates the coordinate
10 systems for in-plane measurements of the reference film and patterned devices. 0 degree corresponds to the anchor direction of ME
11 antennas.

12

13 To evaluate the magnetic anisotropy of FeGaB/SiO₂ multilayers, room temperature magnetic magnetisation loops are measured along
14 the 0 and 90 degrees axes and shown in Fig. 2b and e for the full film and the SMR device. A clear presence of a well-defined in-
15 plane uniaxial magnetic anisotropy (UMA) is seen in the reference film (Fig. 2b). A small coercive field of 112 A/m with an estimated
16 effective in-plane anisotropy field H_k of ~ 1440 A/m are observed. The obtained soft magnetic properties are significant for achieving
17 large piezomagnetic coefficients. Nevertheless, while the magnetic multilayers were directly deposited on ZnO films and patterned
18 for ME antennas, the magnetic anisotropy field decreases to $H_k \sim 1120$ A/m (Fig. 2e), but also displaying soft magnetic properties. In
19 order to identify the orientation of the effective magnetic anisotropy axis and to obtain more quantitative information, the angular
20 dependence of the in-plane FMR fields was measured. A clear twofold distribution can be seen in Fig. 2c and f from the FMR data
21 for both reference films and ME antennas, which is a characteristic feature of UMA. The angle of the axis and strength of the
22 anisotropy field H_k is determined by fitting the obtained FMR field values H_r with the following function: $H_r = 2 H_K * \sin^2(\varphi - \theta) + H_0$, where H_K is the anisotropy field, φ is the angle of the applied DC magnetic field, θ is the tilt of the UMA axis
23 relative to the 90 degrees axis, and H_0 is a constant field defined by the chosen fixed resonance frequency. The obtained magnitude
24 of H_K and the tilt of the effective magnetic anisotropy axis is 1920 A/m and 12.8 degrees for the reference film and 720 A/m and 11.3
25 degrees for the ME antenna.

27

1 The source of UMA can be in principle attributed to magnetocrystalline anisotropy, substrate surface topography, magnetic field
2 induced anisotropy and stress induced anisotropy³⁸. Due to the amorphous structure of the thick seed layer and smooth substrate
3 surface, we assume only contributions from the induced anisotropies to the UMA. Wang et al.³⁸ demonstrated the stress-induced
4 UMA in FeCoC films. However, the deposited film stress was not analysed. In the current work, a detailed investigation on the
5 anisotropic stress of FeGaB films is carried out and shown in Supplementary Fig. 1, which suggests an additional stress-induced
6 UMA from the initial layers during growth.

7

8 The general magnetic anisotropy alignment is confirmed by spatially resolved magnetic analysis of an identical device (Fig 2 g-h and
9 Supplementary Fig. 6). The magnetic domains walls tend to align roughly along the ~90 degrees axis. Despite the exhibited roughness
10 of the samples, the magnetic anisotropy alignment is still determining the magnetic microstructure. Deviations of the domain wall
11 alignment are related to the laminated structure of the multilayer. This and the observed wide magnetic domain walls, an indication
12 of low magnetic film coupling, confirm the quality of the film structure. Noticeable is the curving of the magnetisation from the edges
13 are caused by stress relaxation³⁹, leading to a stress-induced anisotropy contribution aligned parallel to edges. This indicates tensile
14 stress for the positive magnetostrictive films. This further transfers into a change of the magnetic anisotropy strength in the more
15 central region of the disc shaped device, leading to a spatially varying anisotropy strength alteration. Another factor that plays a role
16 is the change of the magnetic properties in the anchor region, visible from the analysis of the magnetisation process (Supplementary
17 Fig. 6). Overall, the tilt of magnetic anisotropy and the change of integral anisotropy strength of the patterned device structure relative
18 to the full film can be related to spatially varying stress induced anisotropy contributions and the effect of roughness on the coercivity
19 of the sample is not significant in this case.

20

21 **Design and simulations of the SMR-based ME antenna**

22 Prior to fabricating SMR devices, various simulation methods were implemented to design and optimise the performance of SMR-
23 based ME antennas with a focus on the Bragg reflector and ME composites. The first analysis was carried out by using the 1D
24 Mason's model to estimate the reflection coefficient frequency response of a carefully arranged Bragg reflector^{40, 41, 42}. The equivalent
25 circuit model of the SMR-based ME antenna analysed by the Mason's model and based on the transmission line theory is shown in
26 Fig. 3a. The load acoustic impedance decreases while the total number of Bragg reflector layers (n) increases. Therefore, a large value
27 of n is desired for the resonator structure. Typically, three pairs of low/high acoustic impedance layers (n = 6) are chosen for SMRs.

28

1 In order to correlate the working frequency bandwidth of the Bragg reflector with the resonant frequency of the piezoelectric resonator,
2 the thickness of each layer is decided by the equation: $d_{acoustic} = v_{acoustic}/4f$, where $d_{acoustic}$ and $v_{acoustic}$ are the thickness and
3 acoustic velocity of the Bragg reflector layers, respectively. In this work, the working frequency of SMR-based ME antenna was not
4 specified. Therefore, the thickness of each layer was not exactly a quarter wavelength of the acoustic wave. The simulated reflection
5 coefficient of the designed Bragg reflector consisting of three pairs of SiO₂/W layers was calculated. The results of which are shown
6 in Fig. 3b. The total reflection seen from the resonant structure is formed over a wide frequency range from 1 to 3 GHz. The influence
7 on the reflection coefficient with varying number of periods is also exploited and displayed in Fig. 3b. As more periods are applied,
8 more energy is reflected from Bragg acoustic lattice, and so the frequency band widens. The calculation results for more periods of
9 SiO₂/W layers are presented in Supplementary Fig. 3, which illustrates minimal improvement in the reflection coefficient when the
10 number of periods exceeds three.

11

12 To achieve a frequency domain analysis of the admittance spectrum, a 2D model of the ME antenna was developed, and the coupling
13 between electrical potential and mechanical displacement in the antenna was simulated by the finite element method (FEM) in
14 COMSOL Multiphysics v5.1⁴². The magnitude of the total displacement profile of the longitudinal waves and the standing wave
15 amplitude as a function of depth of the designed ME antenna at the electromechanical resonant frequency of 1.7 GHz are presented
16 in Fig. 3c and d. The 2D strain assumption is used in this model and the thickness of each layer is defined with the value as shown in
17 Supplementary Table 1. The developed Bragg reflector is shown with optimised performance as the acoustic wave energy is well
18 confined within the ME composites with little energy dissipating into the substrate. The return loss curve of the ME antenna is plotted
19 in Fig. 3e, which is achieved by the frequency domain analysis with the 2D FEM COMSOL model. The thicknesses of each individual
20 layer in the Bragg reflector and ME composites determines the working frequency of SMR antenna. As explained previously, the
21 performance of SMRs can be improved by adjusting the thickness of the Bragg reflector layer to be a quarter wavelength of the
22 acoustic wave.

23

24 **Mechanical ME antenna performance**

25 The antenna gain was characterised in an anechoic chamber by utilising a calibrated linear polarisation standard horn antenna. As
26 shown in Fig. 4a, the return loss curve (S_{11}), receiving (S_{12}) and transmitting behaviour (S_{21}) of the SMR antenna with a resonant
27 frequency of 1.75 GHz and antenna gain of -18.8 dBi are presented. The S_{12} and S_{21} curves overlap with each other. The

1 electromechanical resonance frequency, which is defined by the thickness of the ME disk and is validated by the 2D COMSOL model,
2 is expressed as:

3

$$f_0 \propto \frac{1}{2T} \sqrt{\frac{E}{\rho}}, \quad (1)$$

4 where T is the thickness of the ME disk, E and ρ are the equivalent Young's modulus and equivalent density of the resonator,
5 respectively. In Fig. 4b, the schematics and the fitting parameters for the modified Butterworth Van Dyke (MBVD) model with
6 electrical and equivalent mechanical components of SMR antenna are presented. The electromechanical coupling coefficient (k_t^2)
7 and quality factor (Q) are calculated as 1.0% and 95, respectively. The MBVD fitting curve for return loss S_{11} is plotted in Fig. 4c
8 and matches the measurements well. Compared to the released FBAR ME antenna, the SMR antenna has a 10 dBi higher gain. The
9 gain enhancement of the SMR antenna is attributed to the Bragg reflector helping to confine more acoustic energy in the ME films
10 allowing for greater amplitude in EM waves.

11

12 A high linearity is always wanted for the components in the RF systems such as filters, amplifiers and antennas. This is desired
13 because there are numerous different bands, and they have to be protected from any undesired signals. Furthermore, nonlinearity of
14 the devices can undesirably degrade the performance of the system. It has been reported that the acoustic resonators exhibit a nonlinear
15 behaviour at high power levels^{43, 44, 45}. Since the power density and temperature play significant roles in controlling the nonlinearity,
16 various methods such as the device structure, area and materials etc. are used to improve the linearity of acoustic resonators⁴⁶.

17

18 The power handling capability of the FBAR and SMR antennas are characterised by the power sweep results shown in Fig. 4f. The
19 P1dB is acquired by measuring the S_{21} curves as a function of input power. The FBAR antenna has a P1dB of 7.1 dBm while the
20 P1dB of SMR antenna is 30.4 dBm, which shows a better power handling capability of the SMR antenna. The S_{11} curves of the FBAR
21 and SMR antennas at different input power levels are measured and shown in Fig. 4d and e. The resonance peak of the FBAR antenna
22 shifts to lower frequency at high input power while the SMR antenna remains unchanged, which means the FBAR antenna starts
23 going into nonlinear region. This can be explained by the self-heating effects at high power levels. As the input power extremely
24 increases, the high power density leads to self-heating of the resonator and higher temperature. Compared to the free-standing FBAR
25 membrane structure, the SMR antenna with acoustic Bragg reflector stacks has a larger thermal conductivity. This compensation
26 effect results in a better power handling capability. The comparison of performance metrics between the FBAR and SMR antennas
27 are listed in Table 1.

The radiation characteristics of the SMR-based ME antennas were tested in a far-field configuration with a distance of 0.76 m between the SMR antenna and the horn antenna. The active radiative element of the SMR antenna is defined by the ZnO/FeGaB ME heterostructure disk with a diameter of 200 μ m. Owing to the small size of the SMR antenna and the limitations of the probe station, we were only able to measure the in-plane radiation pattern 180 degrees around the SMR device. The schematics and measured radiation pattern are shown in Fig. 5a. A dipole-like radiation pattern is assumed according to the symmetry of the SMR antenna. The radiation pattern shows an approximate 7-degree shift from the centre of the horn antenna due to the in-plane tilt of the UMA, as shown in Fig. 2. The maximum gain is located along the tilted direction of the anchor length (the 7-degree point as shown in Fig. 5e), which is the hard axis (H.A.) of the magnetostrictive FeGaB film. At 7 degrees, the RF magnetic field component of EM wave is parallel to the magnetisation of the magnetostrictive layer, which results in maximum coupling efficiency between the SMR antenna and EM wave to achieve maximum gain. When in-plane radiation is measured at 97 degrees from the centre, the antenna gain approaches its null value because the RF magnetic field is perpendicular to the magnetisation.

The polarisation behaviours of SMR ME antennas were measured by rotating the standard horn antenna along three major axes, as shown in Fig. 5b-d. In the schematic representations of Fig. 5, the horn antenna was rotated along the out-of-plane axis (Fig. 5b), in-plane axis perpendicular to the anchor direction (Fig. 5c) and in-plane axis along the anchor direction (Fig. 5d). The sinusoidal wave along 0° and 180° in all the schematics indicates the RF H-field component of the EM waves from the horn antenna. The normalised gain plot in Fig. 5f-h show a similar shape of bifold symmetry, which results from the in-plane uniaxial magnetic anisotropy of the FeGaB/ZnO multilayer in the resonating disk of the SMR antenna.

As presented in Fig. 5f, the highest gain of the SMR antenna is achieved along the easy axis (E.A.) when the H_{rf} is parallel to the E.A. direction. The lowest gain is measured tilted away from the 0-degree position when the H_{rf} is parallel to the H.A. direction. The other two polarisation charts in Fig. 5g and h show a similar behaviour where the maximum gain is obtained along the E.A. direction of magnetic anisotropy. This is because the strongest coupling between H_{rf} and SMR ME antenna is achieved when H_{rf} is parallel to the magnetic easy axis in the ME disk. The measured results in Fig. 5 demonstrate that the strong coupling between the H-field component of EM waves and the magnetostrictive phase of FeGaB/ZnO heterostructures in SMR antenna will ultimately improve ME antenna gain.

1

2 Conclusion

3 The latest mechanically driven antennas have pushed the boundaries of antenna miniaturisation to micrometre dimensions starting
4 with the free-standing membrane FBAR design. The presented SMR structures for ME antennas not only improve upon the antenna
5 performance metrics but also simplifies the process with better device structural integrity and removing the extra packaging steps
6 required for device protection. We have demonstrated a working micro-sized ME antenna that takes advantage of a solidly mounted
7 resonator to confine energy in the magnetostrictive/piezoelectric heterostructure showing improvements in antenna radiation. The
8 SMR ME antenna, with an overall dimension of $700 \mu m \times 700 \mu m$ (L \times W), was designed and optimised with the 1D Mason model
9 and a 2D COMSOL FEM simulation to operate at a resonant frequency of 1.75 GHz and experimentally demonstrated a gain of -18.8
10 dBi. Further improvements can be made by increasing the SMR quality factor and optimising the impedance matching with the signal
11 feedline to the resonator.

12

13 The SMR ME antennas have demonstrated more robust features than its FBAR freestanding membrane counterparts. Due to its small
14 size, high operating frequency, high sensitivity, structural stability, semiconductor processing integration, and good power handling
15 capability, it is the ideal device for small-size microwave antennas and remote wireless sensing applications used for compact UAVs
16 (unmanned aerial vehicles), bio-implantable antennas, wearable antennas, IoT (internet of things), NFC (near field communication),
17 RFID (radio frequency identification), satellites, and many more existing and to be envisioned applications.

18

19 Methods

20 Methods and any associated references are available in the online version of the paper.

21 Received: ; Accepted: ; Published online:

22

23 References

- 24 1. He Y, Pan Z, Cheng X, He Y, Qiao J, Tentzeris MM. A novel dual-band, dual-polarized, miniaturized and low-profile base
25 station antenna. *IEEE Transactions on Antennas and Propagation* **63**, 5399-5408 (2015).
- 26 2. Lizzi L, Ferrero F, Monin P, Danchesi C, Boudaud S. Design of miniature antennas for IoT applications. In: *2016 IEEE*
27 *Sixth International Conference on Communications and Electronics (ICCE)*. IEEE (2016).
- 28 3. Hong W, Baek K-H, Lee Y, Kim Y, Ko S-T. Study and prototyping of practically large-scale mmWave antenna systems for
29 5G cellular devices. *IEEE Communications Magazine* **52**, 63-69 (2014).

- 1 4. Hong W, *et al.* Multibeam antenna technologies for 5G wireless communications. *IEEE Transactions on Antennas and*
2 *Propagation* **65**, 6231-6249 (2017).
- 3 5. Buell K, Mosallaei H, Sarabandi K. A substrate for small patch antennas providing tunable miniaturization factors. *IEEE*
4 *Transactions on Microwave Theory and Techniques* **54**, 135-146 (2006).
- 5 6. Skrivervik AK, Zurcher J-F, Staub O, Mosig J. PCS antenna design: The challenge of miniaturization. *IEEE Antennas and*
6 *propagation Magazine* **43**, 12-27 (2001).
- 7 7. Gianvittorio JP, Rahmat-Samii Y. Fractal antennas: A novel antenna miniaturization technique, and applications. *IEEE*
8 *Antennas and Propagation magazine* **44**, 20-36 (2002).
- 9 8. Werner DH, Ganguly S. An overview of fractal antenna engineering research. *IEEE Antennas and propagation Magazine*
10 **45**, 38-57 (2003).
- 11 9. Dong Y, Itoh T. Metamaterial-based antennas. *Proceedings of the IEEE* **100**, 2271-2285 (2012).
- 12 10. Wheeler HA. Fundamental limitations of small antennas. *Proceedings of the IRE* **35**, 1479-1484 (1947).
- 13 11. Volakis J, Chen C-C, Fujimoto K. *Small antennas: miniaturization techniques & applications*. McGraw Hill Professional
14 (2009).
- 15 12. Kiourti A, Nikita KS. A review of implantable patch antennas for biomedical telemetry: Challenges and solutions [wireless
16 corner]. *IEEE Antennas and Propagation Magazine* **54**, 210-228 (2012).
- 17 13. Scarpello ML, *et al.* Design of an implantable slot dipole conformal flexible antenna for biomedical applications. *IEEE*
18 *Transactions on Antennas and Propagation* **59**, 3556-3564 (2011).
- 19 14. Kiourti A, Nikita KS. A review of in-body biotelemetry devices: implantables, ingestibles, and injectables. *IEEE*
20 *Transactions on Biomedical Engineering* **64**, 1422-1430 (2017).
- 21 15. Nan C-W, Bichurin M, Dong S, Viehland D, Srinivasan G. Multiferroic magnetoelectric composites: Historical perspective,
22 status, and future directions. *Journal of applied physics* **103**, 1 (2008).
- 23 16. Srinivasan G. Magnetoelectric composites. *Annual Review of Materials Research* **40**, 153-178 (2010).
- 24 17. Sun NX, Srinivasan G. Voltage control of magnetism in multiferroic heterostructures and devices. In: *Spin*). World Scientific
25 (2012).
- 26 18. Liang X, Chen H, Sun NX. Magnetoelectric materials and devices. *APL Materials* **9**, 041114 (2021).
- 27 19. Li M, *et al.* Highly sensitive DC magnetic field sensor based on nonlinear ME effect. *IEEE sensors letters* **1**, 1-4 (2017).
- 28 20. Tu C, Dong C, Chu Z, Chen H, Liang X, Sun NX. A passive isolator realized by magnetoelectric laminate composites.
29 *Applied Physics Letters* **113**, 262904 (2018).
- 30 21. Chu Z, *et al.* A low-power and high-sensitivity magnetic field sensor based on converse magnetoelectric effect. *Applied*
31 *Physics Letters* **115**, 162901 (2019).
- 32 22. Chen H, *et al.* Integrated Tunable Magnetoelectric RF Inductors. *IEEE Transactions on Microwave Theory and Techniques*,
33 (2020).
- 34 23. Liang X, *et al.* A Review of Thin-Film Magnetoelastic Materials for Magnetoelectric Applications. *Sensors* **20**, 1532 (2020).
- 35 24. Yao Z, Wang YE, Keller S, Carman GP. Bulk acoustic wave-mediated multiferroic antennas: Architecture and performance
36 bound. *IEEE Transactions on Antennas and Propagation* **63**, 3335-3344 (2015).

- 1 25. Nan T, *et al.* Acoustically actuated ultra-compact NEMS magnetoelectric antennas. *Nature Communications* **8**, 296 (2017).
- 2 26. Liang X, Chen H, Sun N, Lin H, Sun NX. Novel Acoustically Actuated Magnetoelectric Antennas. In: *2018 IEEE International Symposium on Antennas and Propagation & USNC/URSI National Radio Science Meeting*). IEEE (2018).
- 3 27. Chen H, *et al.* Ultra-compact mechanical antennas. *Applied Physics Letters* **117**, 170501 (2020).
- 4 28. Chen H, Liang X, Sun N, Sun N-X, Lin H, Gao Y. An Ultra-Compact ME Antenna Design for Implantable Wireless
Communication. In: *2020 IEEE International Symposium on Antennas and Propagation and North American Radio Science
Meeting*). IEEE (2020).
- 5 29. Zaeimbashi M, *et al.* Ultra-compact dual-band smart NEMS magnetoelectric antennas for simultaneous wireless energy
harvesting and magnetic field sensing. *Nature Communications* **12**, 1-11 (2021).
- 6 30. Bickford JA, McNabb RS, Ward PA, Freeman DK, Weinberg MS. Low frequency mechanical antennas: Electrically short
transmitters from mechanically-actuated dielectrics. In: *2017 IEEE International Symposium on Antennas and Propagation
& USNC/URSI National Radio Science Meeting*). IEEE (2017).
- 7 31. Selvin S, Prasad MS, Huang Y, Wang E. Spinning magnet antenna for VLF transmitting. In: *2017 IEEE International
Symposium on Antennas and Propagation & USNC/URSI National Radio Science Meeting*). IEEE (2017).
- 8 32. Burch HC, Garraud A, Mitchell MF, Moore RC, Arnold DP. Experimental generation of ELF radio signals using a rotating
magnet. *IEEE Transactions on Antennas and Propagation* **66**, 6265-6272 (2018).
- 9 33. Bickford JA, Duwel AE, Weinberg MS, McNabb RS, Freeman DK, Ward PA. Performance of electrically small
conventional and mechanical antennas. *IEEE Transactions on Antennas and Propagation* **67**, 2209-2223 (2019).
- 10 34. Dong C, *et al.* A Portable Very Low Frequency (VLF) Communication System Based on Acoustically Actuated
Magnetolectric Antennas. *IEEE Antennas and Wireless Propagation Letters*, (2020).
- 11 35. Ruby RC, Bradley P, Oshmyansky Y, Chien A, Larson J. Thin film bulk wave acoustic resonators (FBAR) for wireless
applications. In: *2001 IEEE Ultrasonics Symposium. Proceedings. An International Symposium (Cat. No. 01CH37263)*).
IEEE (2001).
- 12 36. Newell W. Face-mounted piezoelectric resonators. *Proceedings of the IEEE* **53**, 575-581 (1965).
- 13 37. McCord J. Progress in magnetic domain observation by advanced magneto-optical microscopy. *Journal of Physics D:
Applied Physics* **48**, 333001 (2015).
- 14 38. Wang J, *et al.* Magnetostriction, Soft Magnetism, and Microwave Properties in Co-Fe-C Alloy Films. *Physical Review
Applied* **12**, 034011 (2019).
- 15 39. McCord J. Irregular domain patterns in structured magnetic thick films. *Journal of applied physics* **95**, 6855-6857 (2004).
- 16 40. Nakamura K, Kanbara H. Theoretical analysis of a piezoelectric thin film resonator with acoustic quarter-wave multilayers.
In: *Proceedings of the 1998 IEEE International Frequency Control Symposium (Cat. No. 98CH36165)*). IEEE (1998).
- 17 41. Cannatà D, *et al.* Nerve agent simulant detection by solidly mounted resonators (SMRs) polymer coated using laser induced
forward transfer (LIFT) technique. *Sensors and Actuators B: Chemical* **173**, 32-39 (2012).
- 18 42. Villa-López FH, Rughoobur G, Thomas S, Flewitt AJ, Cole M, Gardner JW. Design and modelling of solidly mounted
resonators for low-cost particle sensing. *Measurement Science and Technology* **27**, 025101 (2015).
- 19 43. Nosek J. Drive level dependence of the resonant frequency in BAW quartz resonators and his modeling. *IEEE transactions
on ultrasonics, ferroelectrics, and frequency control* **46**, 823-829 (1999).

- 1 44. Kaajakari V, Mattila T, Oja A, Seppa H. Nonlinear limits for single-crystal silicon microresonators. *Journal of*
2 *Microelectromechanical systems* **13**, 715-724 (2004).
- 3 45. Aigner R, Huynh N-H, Handtmann M, Marksteiner S. Behavior of BAW devices at high power levels. *Proceedings of IEEE*
4 *IMS-MTT-S*, (2005).
- 5 46. Schmidhammer E. Nonlinear effects in acousto-electric devices. In: *2008 4th European Conference on Circuits and Systems*
6 *for Communications*). IEEE (2008).
- 7
8
9
10
11

12 **Methods**

13 **Materials decision.** The acoustic impedance of various materials is the key point for creating effective Bragg reflectors used for
14 ME antennas. Silicon (Si), silicon dioxide (SiO_2) and aluminium (Al) are common low impedance materials for Bragg reflectors
15 while platinum (Pt), tungsten (W) and iridium (Ir) are introduced as high impedance materials. In this work, we determined that
16 employing sputtered SiO_2/W as the low/high acoustic impedance materials to construct the Bragg reflector will provide the best
17 acoustic impedance ratio along with a cost-effective fabrication process. In order to achieve strong ME coupling in the
18 magnetostrictive/piezoelectric ME composites, ferromagnetic/ferroelectric materials with large piezomagnetic/piezoelectric
19 coefficients are desired. Excellent magnetic softness and magnetostrictive behaviours have been realised in FeGa-based thin films^{47,}
20 ⁴⁸, which have already been applied in different RF/microwave tuneable devices^{22,25}. Aluminium nitride (AlN) and zinc oxide (ZnO)
21 are two of the most popular piezoelectric materials for FBAR devices, among which, AlN has been chosen as the material for
22 commercial BAW filters that operates at 1-2 GHz because of its quality factor (Q). However, ZnO has larger K_t^2 and wider
23 bandwidth than AlN due to its higher piezoelectric coefficient (d_{33}). Moreover, the deposition, control of texture, and stoichiometry
24 of ZnO is much easier compared with that for AlN^{49,50}. ZnO films with highly c-axis-preferred orientation are essential for realising
25 high-quality SMR-type ME antennas. To fabricate SMR-based ME antennas, SiO_2/W as the low/high impedance Bragg reflector
26 and FeGaB/ZnO as the magnetostrictive/piezoelectric ME composite were carefully designed and deposited by RF magnetron
27 sputtering. Platinum (Pt) and gold (Au) were chosen as the bottom and top electrodes, respectively, due to the benefits for growing
28 highly c-axis-textured ZnO thin films and decent conductivity.

29

30 **Thin films deposition.** All thin-film materials were prepared in a magnetron sputtering system at the Argon (Ar) flux density of 15
31 sccm with a base pressure of $\sim 1 \times 10^{-7}$ Torr. The oxides including SiO_2 and ZnO were deposited by reactive RF sputtering and
32 other metallic thin films involving W, FeGaB, Pt, and Au were DC sputtered. All materials were deposited at room temperature
33 except ZnO layer, which was deposited at 450 °C to achieve a highly c-axis-orientated structure. For the Bragg reflector with
34 structure of [W (531 nm)/ SiO_2 (543 nm)]₃, W layers were sputtered at a plasma power of 50 W and an Ar atmosphere of 4.5 mTorr;

1 SiO₂ layers were deposited by reactive RF sputtering from a Si target with a 10:1 Ar/O₂ gas mixture at a plasma power of 75 W and
2 a sputtering pressure of 6 mTorr. For the piezoelectric/magnetostrictive ME composite, the piezoelectric ZnO layer was prepared
3 by reactive RF sputtering from a Zn target with a 3:1 Ar/O₂ gas mixture at a plasma power of 150 W and a sputtering pressure of 3
4 mTorr; the magnetostrictive multilayer with the structure of [FeGaB (85 nm)/SiO₂ (5 nm)]₁₀ was deposited on a 10 nm Cr seed layer
5 at a plasma power of 50 W and a sputtering pressure of 3 mTorr. The FeGaB and SiO₂ layers were sputtered from a (Fe₈₀Ga₂₀)₈₈B₁₂
6 (DC sputtering) target and a SiO₂ (RF sputtering) target, respectively. Ti (5 nm)/Pt (50 nm) and Cr (5 nm)/Au (100 nm) electrodes
7 were prepared at 30 W and 3 mTorr. X-ray reflectivity method was used to calibrate the deposition rates.

8

9 **Device fabrication.** A high resistivity (>10000 Ω · cm) Si wafer was chosen to begin the process. The Bragg reflector consisting of
10 three pairs of W/SiO₂ layers was sputter-deposited in one run with RF reactive magnetron sputtering for SiO₂ and DC sputtering for
11 W in our PVD system. A 50-nm-thick Pt film was sputter-deposited and patterned by lift-off on top of the Bragg reflector to establish
12 the bottom electrodes. Then, the ZnO film was sputter-deposited by RF reactive sputtering with Zn target and high-purity O₂ gas and
13 vias were etched by Hydrochloric (HCl) acid to access the bottom electrodes. After that, a 100-nm-thick Au film was sputtered and
14 patterned by lift-off to form the top ground electrode. Finally, the FeGaB/SiO₂ multilayer layer was deposited by a magnetron
15 sputtering and patterned by lift-off. A 2.4×10^4 A/m in-situ magnetic field bias perpendicular to the anchor direction of the device
16 was applied during the magnetic deposition to pre-orient the magnetic domains. The 3D exploded view of four-masks
17 microfabrication process and SMR-based ME antennas layout can be found in Supplementary Fig. 4. The performance of a fabricated
18 SMR antenna with a resonator diameter of 200 μm was characterised.

19

20 **FMR and MOKE measurements.** An electron paramagnetic resonance spectrometer operating at X-band (9.6 GHz) with a TE₁₀₂
21 microwave cavity was utilised to characterise the in-plane angular dependence of FMR field for the reference full film and patterned
22 device. The DC magnetic field was applied in the film plane and perpendicular to the magnetic component of the microwave field.
23 Magnetooptical Kerr effect (MOKE) microscopy³⁹ in the longitudinal mode was employed for the analysis of the magnetisation and
24 magnetic domain behaviour in the SMR-based ME devices. An illumination wavelength of 460 nm was used for the MOKE imaging
25 in combination with a differential imaging technique for low magnetooptical signal detection. The in-plane magnetic sensitivity
26 was varied for obtaining complementary magnetic domain and magnetic domain wall magnetooptical contrast. The in-plane applied
27 magnetic field direction is freely rotatable and was varied during the experiments.

1
2 **S parameters measurement.** The SMR antennas and horn antenna are connected to port 1 and 2 of a vector network analyser
3 (VNA) (Agilent E8364A) in order to measure the return loss and transmission curves. Before measuring the devices, a short-open-
4 load-through calibration was performed. For various setting parameters of the VNA, the output power was -12 dBm and the
5 intermediate frequency (IF) was set to 500 Hz. A home-made 3D-printed plastic RF probe station with configured ground-signal-
6 ground probes was utilised to test the devices. All SMR antennas are fabricated and characterised in a 15 x 15 mm² chip due to their
7 small size of 0.7 x 0.7 mm².
8

9 **1D Mason model calculation.** The equivalent circuit structure (Fig. 3a) contains the Si substrate, the Bragg reflector (3 pairs of
10 alternating W/SiO₂ layers), and the piezoelectric ZnO film sandwiched between the bottom Pt electrode and the magnetostrictive
11 FeGaB/SiO₂ multilayers. As noted in the equivalent circuit, Z is the acoustic impedance, k is the propagation constant, and d is the
12 layer thickness. Subscripts m, p, e, l, h and s denote the magnetostrictive, piezoelectric, bottom electrode, low acoustic impedance,
13 high acoustic impedance and substrate layers, respectively. Additionally, C₀ is the static capacitance of the piezoelectric resonator; A
14 represents the electrode area; ε₃₃ and e₃₃ are the dielectric and piezoelectric constants of the piezoelectric layer; Y_{in} is the input
15 admittance of the electric port. The effective load acoustic impedance to the resonator seen from the interface between the Bragg
16 reflector and bottom electrode is:

$$Z_{load} = \begin{cases} \left(\frac{Z_l}{Z_h}\right)^{n-1} \left(\frac{Z_l^2}{Z_s}\right) & (n : odd) \\ \left(\frac{Z_l}{Z_h}\right)^n Z_s & (n : even) \end{cases}, \quad (1)$$

17 where n is the total number of Bragg reflector layers.
18

19 **Finite element analysis of electromechanical properties.** To analyse the resonance mode and displacement of the SMR device,
20 piezoelectric module in COMSOL Multiphysics v5.1 was used for the electromechanical simulation²⁵. The modules of solid
21 mechanics and electrostatics were carried out to investigate its performance. The simulation was performed at the frequency domain
22 in a 2D geometry. For the piezoelectric ZnO layer, a small signal behaviour can be described by constitutive relations in the PZD
23 modules. The fixed constraint condition is applied to the edges of the structure and all other boundaries are set as free. The bottom Pt
24 electrode is set as the ground and the electrical potential of terminal is set to 1.0 V, which is applied to the top magnetostrictive layer.
25

1 A mapped mesh with different distributions is used to form the meshing of SMR-based ME antenna. More details of the analysis can
2 be found in reference [26].

3

4 **MBVD model fitting.** MBVD model as shown in Fig. 4b is utilised to extract the electromechanical parameters: k_t^2 and Q-factor. k_t^2
5 denotes the conversion efficiency between electrical and acoustic energy; Q-factor represents the ratio of energy stored and dissipated
6 in the resonator. R_s represents the ohmic losses in the electrodes; R_m , L_m , and C_m are the motional resistance, inductance and
7 capacitance, respectively; R_0 and C_0 are related to the dielectric losses of the piezoelectric layer. The k_t^2 and Q-factor are defined as:

8

$$k_t^2 = \frac{\pi^2 C_m}{8 C_0}, \quad (2)$$

9

$$Q = \frac{8}{\pi^2 R_m} \sqrt{\frac{L_m}{C_m}}, \quad (3)$$

10

11 **Antenna gain calculation.** Through the gain-transfer (gain-comparison) method, the gain of SMR antennas at the resonance
12 frequency f_0 is expressed as:

13

$$G_{SMR} = G_R + S_{21,SMR} + S_{21,R}, \quad (4)$$

14 where G_R is the gain of the reference antenna, $S_{21,SMR}$ and $S_{21,R}$ are the transmitting S parameters of SMR antenna and reference
15 antenna. GR of the horn antenna is 10.6 dBi at 1.75 GHz.

16

17 **Data availability**

18 All relevant data in the article are available from the corresponding author on reasonable request.

19

20 **References**

- 21 47. Lou J, Insignares R, Cai Z, Ziener KS, Liu M, Sun NX. Soft magnetism, magnetostriction, and microwave properties of
22 FeGaB thin films. *Applied Physics Letters* **91**, 182504 (2007).
- 23
- 24 48. Liang X, *et al.* Soft Magnetism, Magnetostriction and Microwave Properties of Fe-Ga-C Alloy Films. *IEEE Magnetics
Letters*, (2018).
- 25
- 26 49. Pearton S, Norton D, Ip K, Heo Y, Steiner T. Recent progress in processing and properties of ZnO. *Progress in materials
science* **50**, 293-340 (2005).
- 27
- 28 50. Fu YQ, *et al.* Recent developments on ZnO films for acoustic wave based bio-sensing and microfluidic applications: a
29 review. *Sensors and Actuators B: Chemical* **143**, 606-619 (2010).
- 30
- 31

1

2 **Acknowledgements**

3 The financial supports from the NSF TANMS ERC Award 1160504, W.M. Keck Foundation. Special thanks to Dr. Mohan
4 Sanghadasa at U.S. Army Combat Capabilities Development Command Aviation & Missile Center for their support. Army SBIR
5 program award # W9113M-19-C-0063. The UIUC team acknowledges support from Office of Naval Research (ONR) MURI through
6 grant N00014-16-1-2436. The Kiel team acknowledges support from the German German Research Foundation (Deutsche
7 Forschungsgemeinschaft, DFG) through the Collaborative Research Centre CRC 1261 “Magnetolectric Sensors: From Composite
8 Materials to Biomagnetic Diagnostics”. The picosecond acoustics experiments were carried out in the Materials Research Laboratory
9 Central Research Facilities, University of Illinois.

10

11 **Author contributions**

12 X.L., H.C., and N.S. made the preliminary experimental observations. X.L., H.C., N.S., and N.X.S. conceived and designed the
13 experiments. X.L., H.C., and N.S. conducted the experiments and characterisations, analysed the data with the help of C.M., E.G.,
14 S.M., Y.W., C.D., M.Z., Y.H., M.S., Y.G., H.L., D.G.C., and J.M.. The first manuscript was drafted by X.L. and N.X.S. with inputs
15 from all the other authors.

16

17 **Competing interests**

18 The authors declare no competing financial interests.

19

20 **Additional information**

21 Supplementary information is available in the online version of the paper.

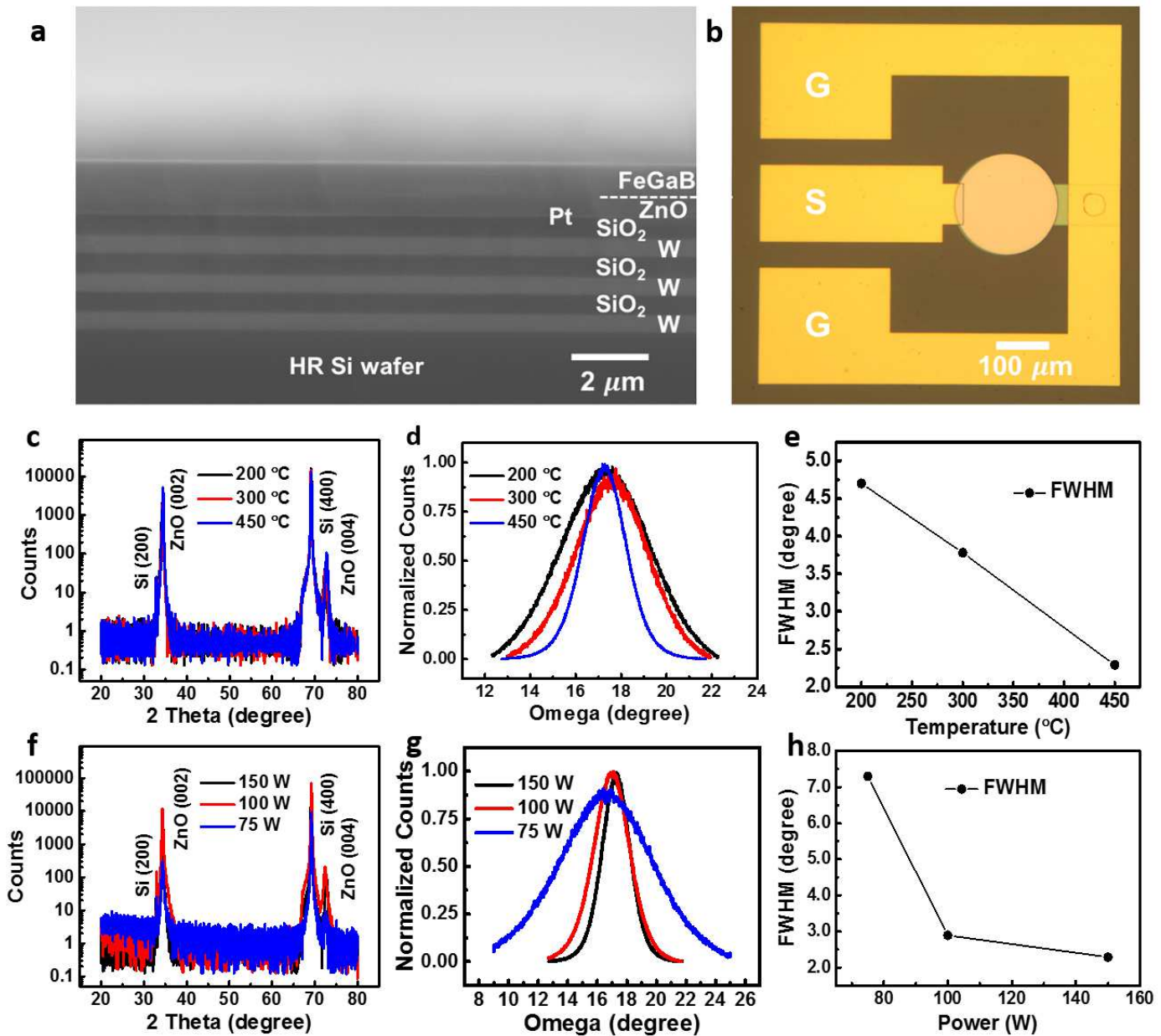
22 Correspondence and requests for materials should be addressed to Nian X. Sun.

23 Reprints and permissions information is available online at www.nature.com/reprints.

24 Publisher's note: Springer Nature remains neutral with regard to jurisdictional claims in published maps and institutional affiliations.

1

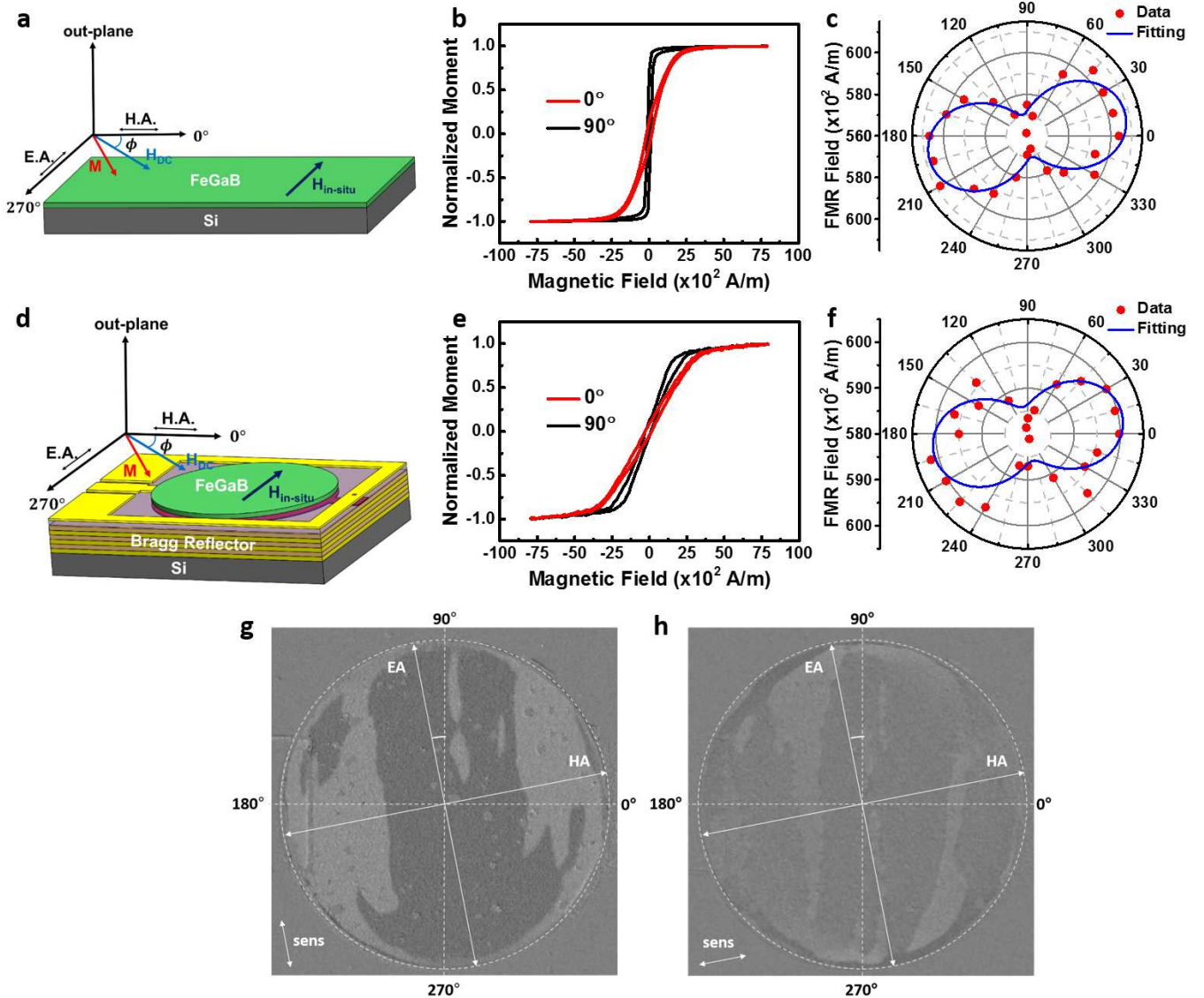
2 Figures and tables



3

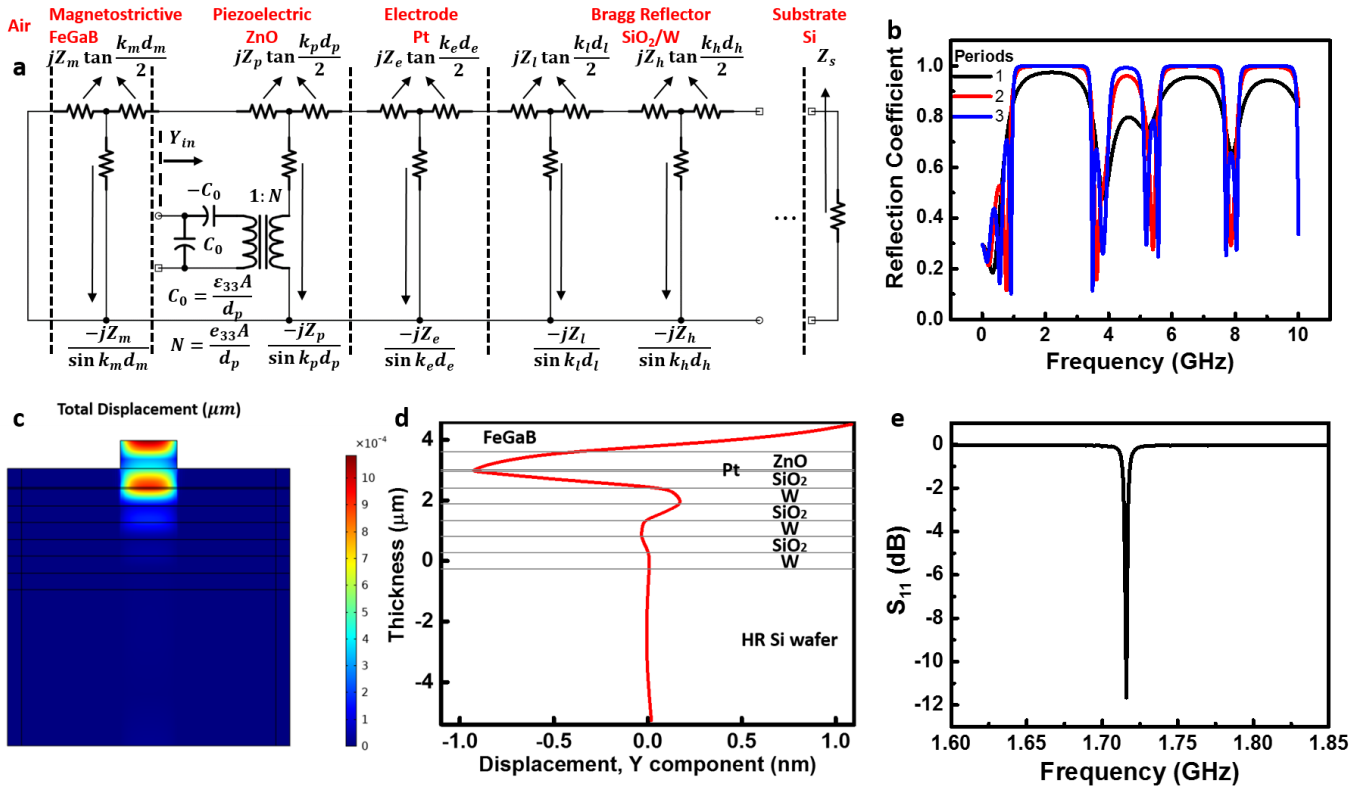
4 **Fig. 1 | Structural properties of the fabricated SMR ME antenna.** **a**, Cross-sectional SEM image of the ME antenna. **b**, Optical
 5 image of the ME antenna. Ground (G) and signal (S) pads are used to feed the RF signal into the device. **c**, **f**, XRD patterns of ZnO
 6 films with increasing deposition temperature and RF plasma power. **d**, **g**, Rocking curves of ZnO films with increasing deposition
 7 temperature and RF plasma power. All curves are fitted with Gauss function to get the FWHM values. **e**, **h**, FWHM versus deposition
 8 temperature and plasma power.

9



1

2 **Fig. 2 | Magnetic properties of FeGaB/SiO₂ multilayers.** **a, d**, Coordinate systems for in-plane analysis of the reference full film
 3 and patterned device. 0° is aligned perpendicular to the in-situ magnetic field. **b, e**, Magnetisation loops for the reference full film
 4 and the patterned device. Black: along the 90-degree axis; Red: along the 0-degree axis. **c, f**, In-plane angular dependence of FMR
 5 fields for the reference full film and patterned device. Red points: experimentally measured data; blue lines: fitted data. **g, h** Remanent
 6 state after magnetic field application aligned along the hard axis of the sample (11-degree axis). MOKE sensitivity is along the 101°
 7 (E.A.) (**g**) and 11° (H.A.) (**h**) axis.



1

2 **Fig. 3 | 1D Mason model and 2D finite element model (FEM) COMSOL simulation results of the proposed SMR-based ME**
 3 **antenna.** **a**, Equivalent circuit of the SMR-based ME antenna analysed by Mason's model. Z_i , k_i and d_i : acoustic impedance,
 4 propagation constant and thickness of each layer; C_0 : static capacitance of the resonator; A : electrode area; ε_{33} and e_{33} are dielectric
 5 and piezoelectric constants of the piezoelectric layer; Y_{in} : input admittance of the electric port. **b**, Simulated reflection coefficient of
 6 the designed Bragg reflector consisting of various pairs of SiO₂/W layers based on the Mason model. **c**, Displacement profile at
 7 resonant frequency. **d**, Standing wave amplitude as a function of depth and **e**, Frequency response of the designed ME antenna
 8 simulated with the 2D FEM COMSOL model.

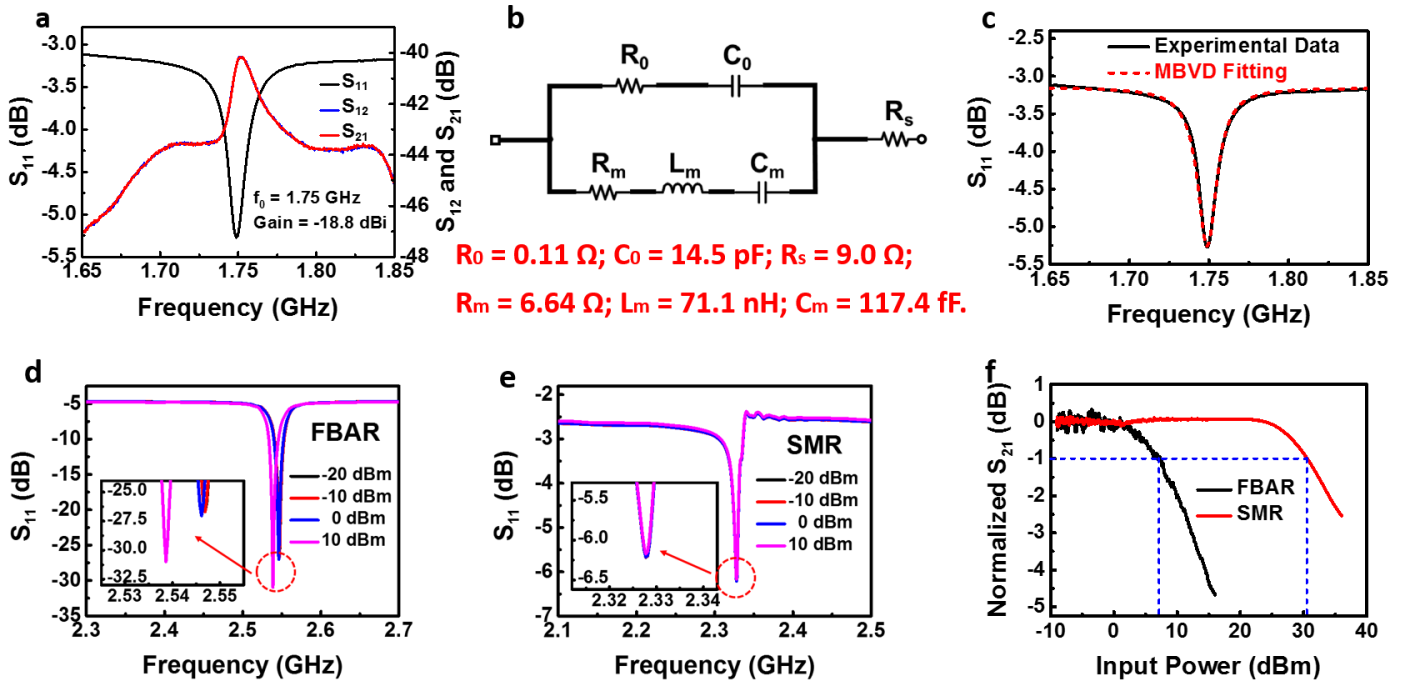


Fig. 4 | Modified Butterworth Van Dyke (MBVD) model and power handling measurements of the SMR antenna. **a**, Return loss curve (S_{11}), receiving (S_{12}) and transmitting behaviour (S_{21}) of the SMR antenna with resonant frequency of 1.75 GHz and antenna gain of -18.8 dBi. **b**, Schematics of MBVD model with fitted values. **c**, Return loss curves (S_{11}) for experimental data and MBVD fitting. **d**, S_{11} results of the FBAR antenna at different input power. The resonance peak shifts to lower frequency with input power of 10 dBm, which means the FBAR antenna goes into nonlinear region. **e**, S_{11} results of the SMR antenna at different input power. The antenna performance is stable without any frequency shift. **f**, Power sweep of the FBAR and SMR antennas. The FBAR antenna has a 1 dB compression point (P_{1dB}) of 7.1 dBm while the P_{1dB} of SMR antenna is 30.4 dBm, which shows the better power handling capability of the SMR antenna.

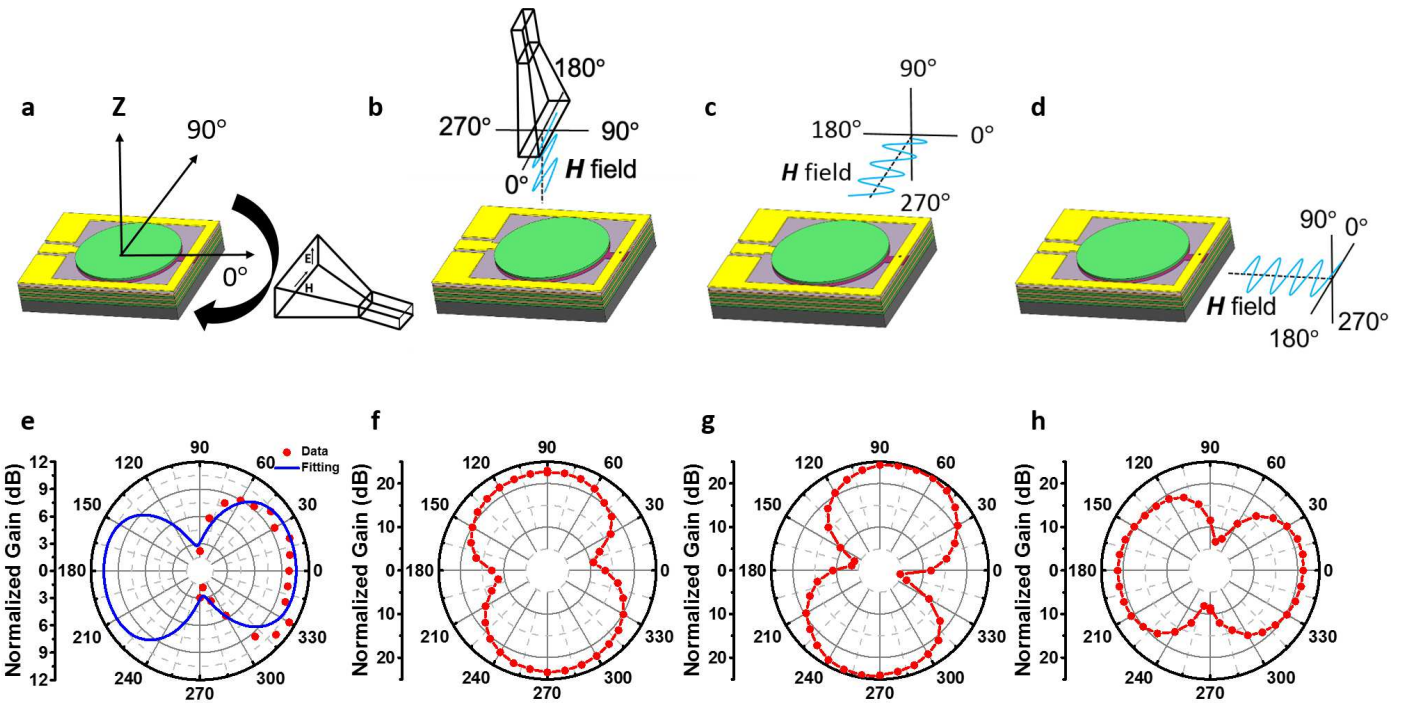


Fig. 5 | Antenna performance of the SMR device. **a-d**, Schematic representations of the test setups for the in-plane radiation pattern and polarisation along three major axes measurements under a calibrated horn antenna. **e**, In-plane radiation pattern. **f-h**, Normalised gain patterns of antenna polarisation for the in-plane rotation, out-of-plane rotation perpendicular the anchor direction and out-of-plane rotation along the anchor direction. The sinusoidal wave along 0° and 180° denotes the H-field component of the EM waves from horn antenna. Red dots represent the experimental data; Blue line is the fitted curve of the cosine function; Red lines are guides for the eyes.

Table 1. Performance comparison between the FBAR and SMR ME antennas.

ME	Frequency	S ₁₁	Gain	P1dB	Process	Robustness
Antenna	(GHz)	(dB)	(dBi)	(dBm)	Control	
FBAR	2.53	< -20	-18	7.1	Hard	Bad
SMR	1.75	~ -5	-18.8	30.4	Easy	Good

9

10

11

Supplementary Files

This is a list of supplementary files associated with this preprint. Click to download.

- [SupplementaryNatureCommunications.pdf](#)